Negating interfacial impedance in garnet-based solid-state Li metal batteries

Xiaogang Han[1†], Yunhui Gong[1†], Kun (Kelvin) Fu[1†], Xingfeng He[1], Gregory T. Hitz[1], Jiaqi Dai[1], Alex Pearse[1,2], Boyang Liu[1], Howard Wang[1], Gary Rubloff[1,2], Yifei Mo[1], Venkataraman Thangadurai[3], Eric D. Wachsman[1]★ and Liangbing Hu[1]★

Garnet-type solid-state electrolytes have attracted extensive attention due to their high ionic conductivity, approaching $1\,mS\,cm^{-1}$, excellent environmental stability, and wide electrochemical stability window, from lithium metal to ~6 V. However, to date, there has been little success in the development of high-performance solid-state batteries using these exceptional materials, the major challenge being the high solid–solid interfacial impedance between the garnet electrolyte and electrode materials. In this work, we effectively address the large interfacial impedance between a lithium metal anode and the garnet electrolyte using ultrathin aluminium oxide (Al_2O_3) by atomic layer deposition. $Li_7La_{2.75}Ca_{0.25}Zr_{1.75}Nb_{0.25}O_{12}$ (LLCZN) is the garnet composition of choice in this work due to its reduced sintering temperature and increased lithium ion conductivity. A significant decrease of interfacial impedance, from $1{,}710\,\Omega\,cm^2$ to $1\,\Omega\,cm^2$, was observed at room temperature, effectively negating the lithium metal/garnet interfacial impedance. Experimental and computational results reveal that the oxide coating enables wetting of metallic lithium in contact with the garnet electrolyte surface and the lithiated-alumina interface allows effective lithium ion transport between the lithium metal anode and garnet electrolyte. We also demonstrate a working cell with a lithium metal anode, garnet electrolyte and a high-voltage cathode by applying the newly developed interface chemistry.

Solid-state lithium batteries (SSLiBs) provide potential solutions to the primary problems encountered in traditional lithium (Li)-ion batteries with liquid electrolytes, such as poor safety, limited voltage, unstable solid-electrolyte interphase formation, and poor cycling performance. Solid-state electrolytes (SSEs) are the enabling material for the successful development of SSLiBs. A range of SSEs have been investigated, such as LiSICON[1], thio-LiSICON[2], NASICON-type Li conductors[3,4], perovskites[5], antiperovskites[6], LiBH$_4$ (ref. 7), sulfide-based glass/ceramic[8,9], garnet[10–14] and so on. Steady progress on the improvement of Li-ion conductivity in SSEs has resulted in record high conductivity of $10^{-2}\,S\,cm^{-1}$ in sulfide-based electrolyte[15], which rivals the conductivity of organic liquid electrolytes. However, for full cell development, a stable interface with small interfacial impedance between SSE and electrodes is critical. Quite a few successful approaches have been applied to reduce interfacial impedance between SSE and cathodes, including surface coating[16–18], interface softening[19,20], and buffer layers, for example, LiNbO$_2$ (ref. 21), Nb[22], BaTiO$_3$ (ref. 16), and additive in cathode composite, for example, LBO[23]. The interface at the anode side, however, has rarely been explored[24], especially when metal Li is used. This is probably due to the fact that many solid electrolytes including perovskite-type (Li, La)TiO$_3$, NASICON (especially Ti-based materials), and sulfide-based glass electrolytes are not stable against metallic Li. Given the fact that Li metal has the highest capacity ($3{,}860\,mAh\,g^{-1}$) and the lowest potential (-3.040 V versus standard hydrogen electrode) for use as an anode, solving the interfacial impedance between the SSE and Li metal is extremely critical for high-energy-density SSLiB development.

Garnet electrolytes are very attractive for SSLiBs because they: have a wide electrochemical window and the most stable interface against Li metal among SSEs[25]; are environmentally stable with much processing flexibility; and have high ionic conductivity, close to $1\,mS\,cm^{-1}$ at room temperature[22,23,26–28]. Since their discovery more than ten years ago, fundamental research has led to both increased understanding of the underlying mechanisms and improved Li-ion conductivity[29–32]. However, there is still little progress on the successful demonstration of high-performance SSLiBs with garnet SSE. One of the major challenges is the large interfacial resistance between garnet electrolyte and electrode materials due to its rigid ceramic nature. Heating or even melting Li metal for its integration with garnet electrolytes has been reported[28]. However, the resistance reduction at the interface was limited, probably due to the poor wetting properties of garnet SSE and molten Li metal which causes microscopic gaps at the interface. Li$_2$CO$_3$ naturally forms on the garnet surface as a source of high interfacial resistance for LLZO with Li metal[33]. After removing surface impurities by polishing, a much lower interfacial area specific resistance (ASR), $\sim\!109\,\Omega\,cm^2$ was successfully achieved. Nevertheless, the achieved interfacial impedance is still too high for SSLiBs, and this polishing approach is only applicable to flat garnet electrolytes, significantly limiting cell geometries and manufacturing scalability.

In this work, we demonstrate that the introduction of an ultrathin Al$_2$O$_3$ coating on garnet-like Li$_7$La$_{2.75}$Ca$_{0.25}$Zr$_{1.75}$Nb$_{0.25}$O$_{12}$ (LLCZN) via atomic layer deposition (ALD) dramatically improves the wetting and stability of garnet SSE, and leads to a significant decrease in interfacial impedance from $1{,}710\,\Omega\,cm^2$ to $1\,\Omega\,cm^2$. Experimental and computation studies are employed to investigate the possible mechanism for the excellent effect of the ALD-Al$_2$O$_3$ coating on the garnet/Li interface improvement. On the basis of

[1]University of Maryland Energy Research Center, and Department of Materials Science and Engineering, University of Maryland, College Park, Maryland 20742, USA. [2]Institute for Systems Research, University of Maryland, College Park, Maryland 20742, USA. [3]Department of Chemistry, University of Calgary, 2500 University Drive Northwest, Calgary, Alberta T2N 1N4, Canada. [†]These authors contributed equally to this work. *e-mail: ewach@umd.edu; binghu@umd.edu
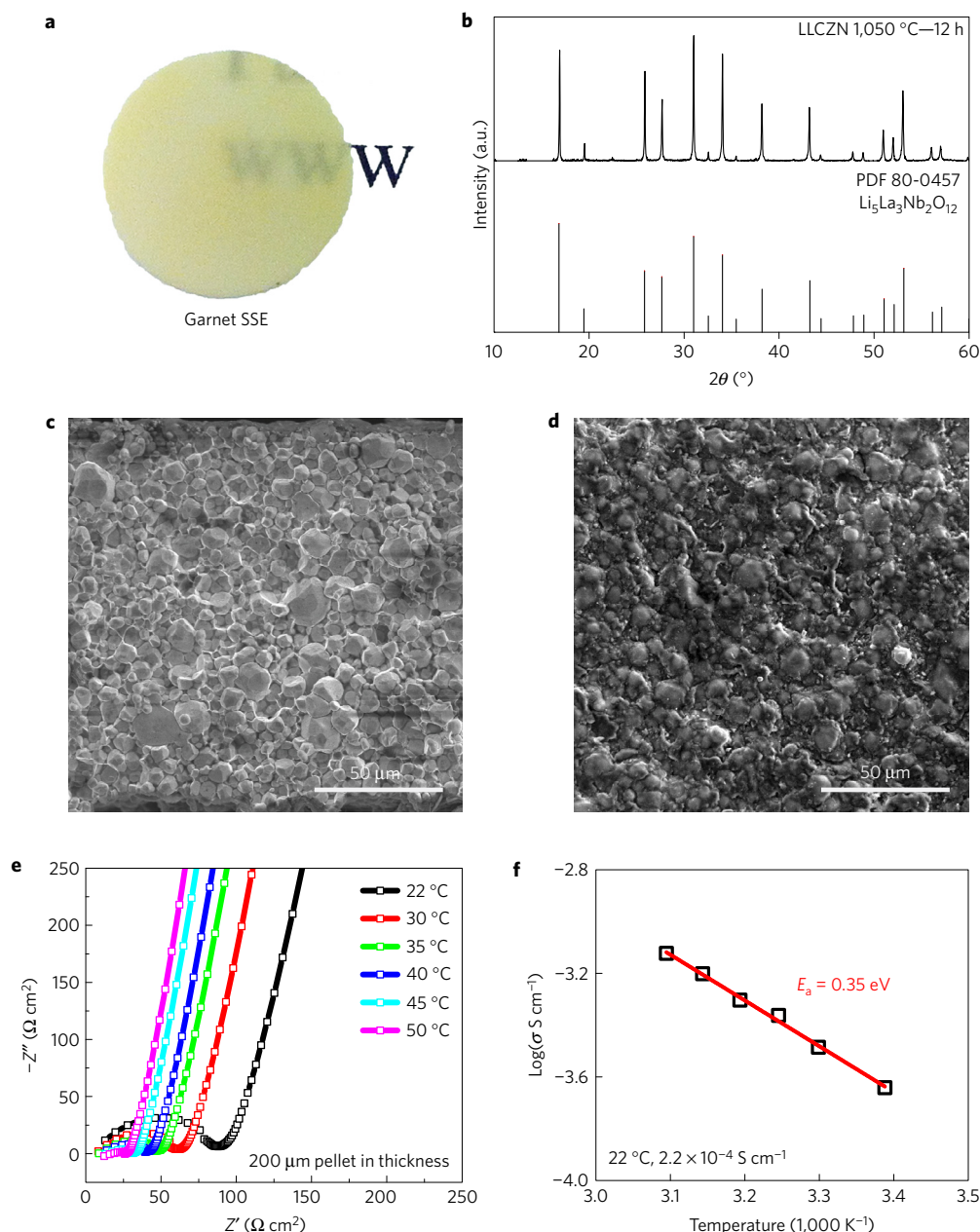
Figure 1 | Characterization of as-prepared LLCZN garnet electrolyte. a, Digital photo of a polished yellowish LLCZN pellet. It is translucent and the underneath letters can be seen. **b**, XRD pattern comparison of the as-prepared LLCZN and standard $Li_5La_3Nb_2O_{12}$ with cubic garnet phase. **c,d**, SEM images for cross-section (**c**) and top view (**d**) of the LLCZN pellet. **e**, EIS of LLCZN pellets at low temperature from 22–50 °C. **f**, Arrhenius plot of the LLCZN ionic conductivity.

this newly developed interface engineering method, a quasi-SSLiB is successfully designed and operated using a Li metal anode, garnet electrolyte and a high-voltage cathode.

Characterization of garnet LLCZN solid electrolyte

Garnet-structured $Li_7La_{2.75}Ca_{0.25}Zr_{1.75}Nb_{0.25}O_{12}$ (LLCZN) was synthesized, sintered and polished into thin solid-electrolyte pellets. The common garnet composition is $Li_7La_3Zr_2O_{12}$ (LLZO), and the simultaneous substitution of the La^{3+} site with Ca^{2+} and the Zr^{4+} site with Nb^{5+} brings merits of reduced sintering temperature, stabilized cubic garnet phase and increased Li-ion conductivity[34]. Figure 1a displays a yellowish LLCZN pellet polished to about 150 µm thick. The thin pellet is translucent and also strong and dense enough for operation. The powder X-ray diffraction (XRD) pattern of the pulverized LLCZN pellet shown in Fig. 1b matches

that of cubic garnet-phase $Li_5La_3Nb_2O_{12}$ (PDF 80-0457), indicating that the LLCZN is pure cubic phase, which has a higher Li-ion conductivity compared with the tetragonal garnet phase. The cross-section scanning electronic microscopy (SEM) image of the LLCZN pellet (Fig. 1c) reveals a dense morphology. Using the Archimedes method with ethanol, the density was determined to be 97% of the theoretical. The different morphology of the top view presented in Fig. 1d is probably caused by impurities inevitably formed in air, such as Li_2CO_3 (ref. 35). For later tests, all of the LLCZN pellets are polished and stored in an argon-filled glovebox.

Li-ion conductivity of the LLCZN was evaluated by electrochemical impedance spectroscopy (EIS) with gold electrodes at temperatures from 22–50 °C. All of the resulting Nyquist plots summarized in Fig. 1e show semicircles at medium frequencies associated with the total resistance from bulk and grain boundary

response, and a connected vertical low-frequency tail corresponding to the capacitive behaviour of Li-ion-blocking gold electrodes. The LLCZN resistance decreases with increasing temperature, and the Arrhenius behaviour for total Li-ion conductivity is plotted in Fig. 1f. The observed activation energy of 0.35 eV and Li-ion conductivity of 2.2×10^{-4} S cm^{-1} at 22 °C are in line with literature values for garnet electrolytes.

Stability of LLCZN contacting Li metal anode

The stability of LLCZN with Li metal anode is important for high-energy-density batteries. The interfacial stability experiments were carried out in an argon-filled glovebox. LLCZN powder was in contact with Li metal at room temperature (22–25 °C) for at least half a year without any visible change (Supplementary Fig. 1). To evaluate the Li/garnet stability at a high temperature, LLCZN powder was thoroughly mixed with molten Li metal in a 1:1 weight ratio at 300 °C for 12 h. Li metal was then removed by washing with methanol several times, and the remaining solid was dried and evaluated using XRD. The featured XRD peaks of the cubic LLCZN are maintained, indicating LLCZN's chemical stability towards Li metal (Supplementary Fig. 2), but slightly shifts to lower angles compared with the pristine LLCZN, which is in agreement with the literature[35]. This shifting indicates an increased lattice parameter, implying the potential for garnet expansion with Li insertion on heating at 300 °C.

The electrochemical stability window of LLCZN was also evaluated using cyclic voltammetry. The results are shown in Supplementary Fig. 3, where an LLCZN pellet was sandwiched between platinum sheet as the working electrode, and Li foil as the reference and counter electrode with slow scan rates (1 mV s^{-1} and 0.05 mV s^{-1}) in a Swagelok cell. The representative redox peaks at about −0.19 V and 0.09 V suggest Li plating/stripping processes with a polarized voltage of ∼0.1 V. No other sensible redox current is observed in the entire test voltage range, suggesting LLCZN's electrochemical stability over a wide voltage window up to 6 V versus metallic Li.

Conformal ALD-Al$_2$O$_3$ interface

We designed a two-step process to achieve a conformal interface on thin garnet pellet LLCZN. First, a 40-ALD-cycle Al$_2$O$_3$ coating was applied to the garnet surface. Then a piece of Li metal foil was pressed on the garnet pellets using a hydraulic press at 50 psi, and then the stacked garnet/Li pellet was heated at 250 °C for 1 h under a small pressure (for details, see Supplementary Information). A control sample was made using bare LLCZN pellets in the same way. It was reported that Li metal cannot wet garnet LLZO until heating for a long time (24–168 h) at a temperature of 300–350 °C (ref. 35), much higher than the Li metal melting point 180.5 °C. Our two-step process to integrate Li metal with garnet at a relatively low temperature causes neither colour centres nor cracks[35]. Figure 2a presents a schematic of the interface between garnet and Li metal. Without surface modification, garnet has insufficient physical contact with Li metal. With the ALD coating, the ultrathin Al$_2$O$_3$ layer helps the molten Li metal to conformally coat the garnet surface with no interfacial void space. The SEM images in Fig. 2b clearly demonstrate the enhancement of interfacial contact by applying the ALD-Al$_2$O$_3$ ultrathin layer on garnet surface. Insets are digital photos to further demonstrate improvement in wetting of ALD-treated garnet.

Li metal–LLCZN interface resistance

To quantify the effect of ALD on the improvement of the garnet/Li interface, symmetric Li/garnet/Li cells were prepared and evaluated by EIS to examine the interfacial resistance. The cells were assembled with otherwise identical procedures and used garnet from the same batch of sintered pellets to maximize consistency and isolate

the effect of ALD. The LLCZN pellets used were 200 μm thick with electrode surface areas of 0.49 cm^2. Samples were measured with EIS at 22 °C to identify individual contributions to the impedance. As shown in Fig. 2c, two distinct arcs were seen in each sample. The bulk ASRs, determined from the high-frequency x-intercepts, are 26 and 28 Ω cm^2 for cells with and without ALD coating, respectively. The first arc represents the overlap of grain boundary and interface impedances, with capacitances of 3.1×10^{-9} F and 2.1×10^{-9} F for cells with and without ALD, respectively. The grain boundary/interface ASRs were found to be 150 Ω cm^2 and 3,500 Ω cm^2 for cells with and without ALD coating, respectively. Since the garnet pellets used in the two cases share an identical origin, the dramatically higher ASR in the non-ALD sample is probably due to poor interfacial contact (Fig. 2b) and an overlap in the grain boundary and Li metal/garnet interfacial impedance frequency dispersion. Interfacial ASR was determined for the interface resistance on either side of the symmetric cells by subtracting the electrolyte resistance from the total cell resistance, dividing by two, and then normalizing to the electrode surface area. The total (bulk and grain boundary) impedance for the LLCZN samples is ∼108 Ω cm^2, which is calculated from the sample thickness and total conductivity obtained by EIS measurements of the Au/garnet/Au blocking electrode symmetric cells (Fig. 1f). The total impedances for the symmetric Li/garnet/Li cells with and without ALD coating are 176 and 3,528 Ω cm^2, respectively. Therefore, the ALD treatment decreased the interfacial ASR by EIS from 1,710 Ω cm^2 to 34 Ω cm^2. The reduction can be possibly attributed to the following reasons: conformal contact of Li metal on SSE increases the effective ionic transfer area; the thermal lithiated Al$_2$O$_3$, formed by contact with Li metal on heating, is Li-ion conductive and effectively transports ions between garnet and Li metal[36]; and the ALD coating layer inhibits impurity, for example, Li$_2$CO$_3$ formation on the garnet surface during processing.

We further carried out d.c. Li plating and stripping experiments to evaluate the interfacial impedance and Li-ion transport capability across the garnet and Li metal interface. At a current density of 0.1 mA cm^{-2}, the Li/LLCZN/Li cell with an ALD coating stabilized at ∼13 mV (Fig. 2d). On the other hand, the control cell without ALD coating displayed a noisy potential with large voltage polarization indicating uneven ion transport through the interface. Figure 2e shows 90 h of cycling at a current density of 0.2 mA cm^{-2} in both directions for 30 min and a stable voltage response at 22 mV. The excellent cycling with small polarization confirms that both low interfacial impedance and a stable interface during Li cycling were obtained with the ALD oxide interfacial layer. The stable interface is possibly due to the high ductility of the lithiated Al$_2$O$_3$, which agrees with literature on the mechanical properties of lithiated and sodiated Al$_2$O$_3$ (refs 37–42). The ASR calculated from the stripping/plating test, based on Ohm's law, is 110 Ω cm^2, close to the total garnet ASR measured by EIS (∼108 Ω cm^2), which indicates the effective removal of the Li/garnet interfacial impedance. The obtained interfacial ASR is therefore only ∼1 Ω cm^2 (calculated by subtracting the overall garnet ASR of ∼108 Ω cm^2 and dividing by two), thus demonstrating that the ALD-Al$_2$O$_3$ coating essentially negated the primary challenge of large interfacial impedance for the practical application of garnet electrolytes with Li metal anodes.

The electrical parameters for the two symmetric cells are summarized in Table 1. Supplementary Fig. 4 shows a comparison of values reported in the literature for interfacial ASR between Li metal and various garnets with ours. As far as we know, this work provides the lowest interfacial ASR among all of the garnet SSE/Li studies[10,33,43–45]. These results clearly suggest that the ultrathin ALD-Al$_2$O$_3$ coating facilitates Li-ion transport through the solid Li/LLCZN interface.
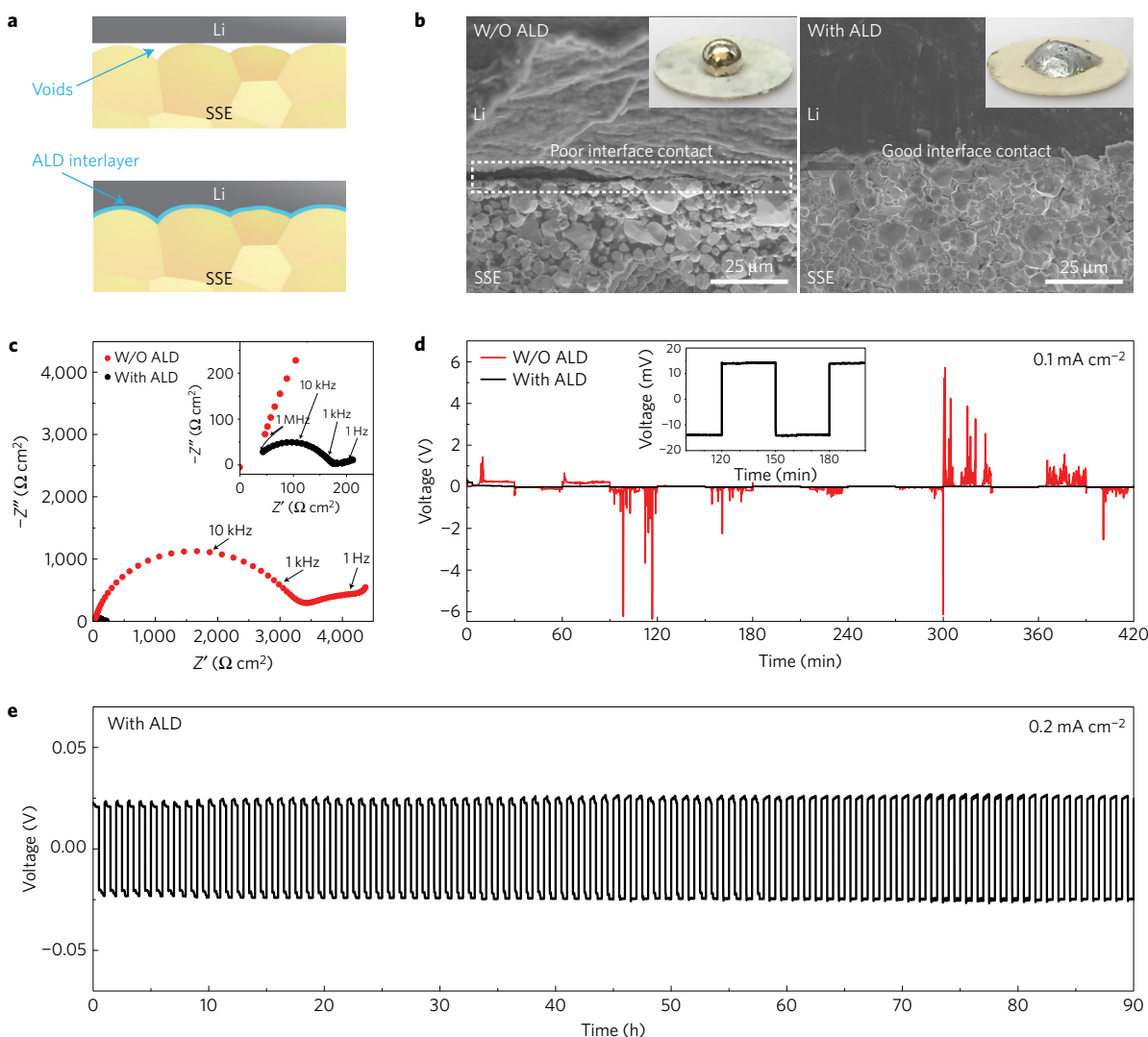
Figure 2 | Characterizations of garnet solid-state electrolyte/Li metal interface. a, Schematic of the wetting behaviour of garnet surface with molten Li.
b, SEM images of the garnet solid-state electrolyte/Li metal interface. Without ALD-Al_2O_3 coating, garnet has a poor interfacial contact with Li metal even on heating. With the help of ALD-Al_2O_3 coating on garnet, Li metal can uniformly bond with garnet at the interface on heating. Inset are photos of melted Li metal on top of the garnet surface clearly demonstrating classical wetting behaviour for the ALD-treated garnet surface. **c**, Comparison of EIS profiles of the symmetric Li non-blocking garnet cells. Inset shows the enlarged impedance curve of the ALD-treated garnet cell. **d**, Comparison of d.c. cycling for symmetric cells of Li/bare garnet/Li (black curve) and Li/ALD-treated garnet/Li (red curve) at a current density of 0.1 mA cm^{-2}. The inset is the magnified curve of the ALD-treated cell. **e**, Galvanostatic cycling of Li/ALD-treated garnet/Li with a current density of 0.2 A cm^{-2}.

Table 1 | Electrochemical impedance and d.c. ASR for Li/LLCZN/Li cells with and without ALD coating on both sides of garnet SSE.

Li/LLCZN/Li symmetric cell	Bulk/high-frequency ASR (Ω cm^2)	GB/interface ASR (Ω cm^2)	Total EIS ASR (Bulk+GB/interface) (Ω cm^2)	Interfacial EIS ASR* (Ω cm^2)	d.c. ASR (Ω cm^2)	Interfacial d.c. ASR* (Ω cm^2)
W/O ALD	28	3,500	3,528	1,710	N/A	N/A
ALD	26	150	176	34	110	1

*Interfacial EIS and d.c. ASR calculated by subtracting total garnet ASR (108 Ω cm^2) from total EIS and d.c. ASR, respectively, and dividing by interfacial area. GB, grain boundary. Garnet ASR (108 Ω cm^2) was obtained from the EIS garnet conductivity measurement of the Au/garnet/Au symmetric cells.

Characterization of ALD coating layer

To understand the ALD-Al_2O_3 layer at the garnet SSE surface, a series of characterizations were carried out. Figure 3 shows the results of transmission electron microscopy (TEM), electron energy-loss spectroscopy (EELS), and selected area electron diffraction (SAED) characterizations for the ALD-Al_2O_3-treated garnet pellets. The TEM sample was prepared by mechanical polishing and then ion milling with a focused ion beam (FIB) at liquid nitrogen temperature. To prevent damage of the ALD-Al_2O_3 coating layer, 10 nm Ti and 2 µm carbon were deposited on the garnet surface before sampling (illustrated in Supplementary Fig. 5). As shown in Fig. 3c,e, the elemental mappings of Al and O overlap, especially at the garnet border (Fig. 3f). When further comparing the relative position of elemental Al, Li and Ti (Fig. 3c,d,g), Al is found to exist between the Ti layer and Li layer, that is, garnet. These results confirm the ALD-Al_2O_3 coating layer on garnet. It
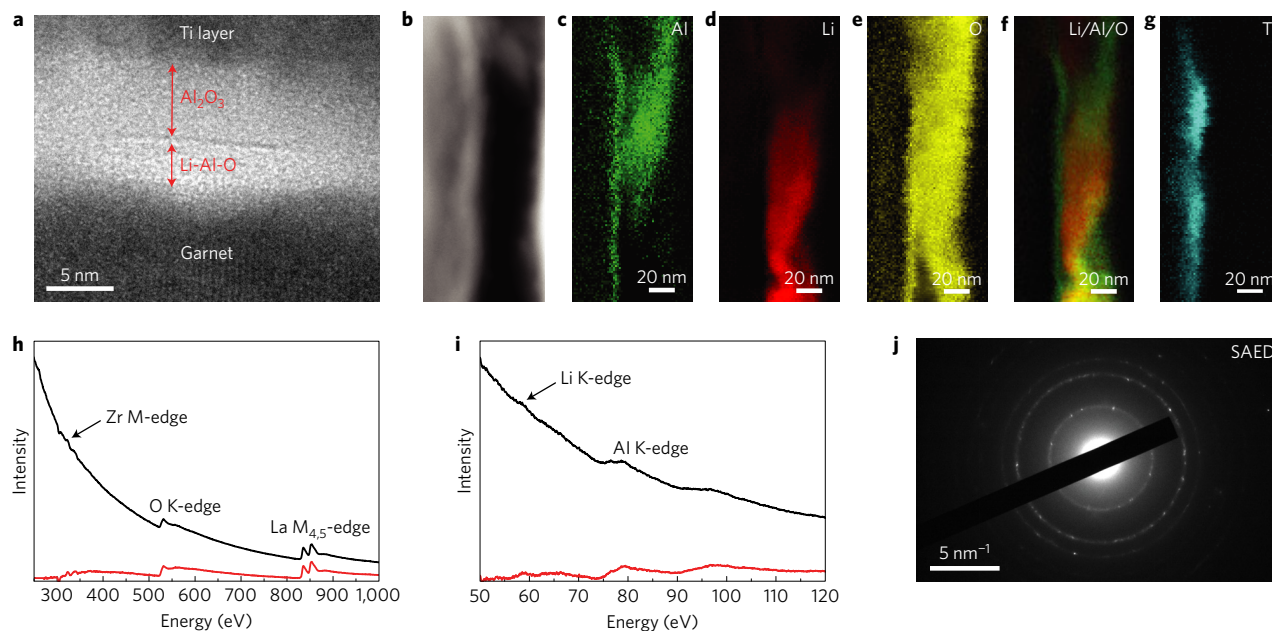
Figure 3 | Characterization for the interface of ALD-Al$_2$O$_3$-coated garnet solid electrolyte. a, Typical TEM cross-section image at the interface of ALD-Al$_2$O$_3$-coated garnet with Ti protection layer. **b–g,** Typical TEM/HAADF image (**b**) and corresponding EELS maps (**c–g**, Al, Li, O, overlap of Al and Li, and Ti, respectively) for the interfacial cross-section. **h,** EELS with energy 250–1,000 eV showing peaks of Zr M-edge, O K-edge, and La M$_{4,5}$-edge. **i,** EELS with energy 50–120 eV showing peaks of Li K-edge and Al L-edge. **j,** SAED of the interlayer between garnet and ALD-Al$_2$O$_3$.

is also observed that Al diffused deeper into the garnet surface (Fig. 3c–f), possibly due to some surface porosity in the garnet (not 100% dense), and some pores were found in the garnet during FIB sampling (Supplementary Fig. 6), thus enabling the Al precursor (gas state) to infiltrate into the garnet pores during the ALD process. The EELS data confirm the existence of the Al$_2$O$_3$ coating layer on the garnet surface.

X-ray photoelectron spectroscopy (XPS) was performed for Al$_2$O$_3$ detection before and after ALD treatment on garnet. As shown in Supplementary Fig. 7, the emergence of the Al 2p peak after ALD treatment further confirms that the Al$_2$O$_3$ on the garnet surface is produced by ALD. After location of the Al$_2$O$_3$ coating layer by EELS mapping, the thickness of the Al$_2$O$_3$ layer was measured to average 5∼6 nm in the typical TEM image (Fig. 3a). This is almost identical to the estimation (5.2 nm) based on the Si wafer control (for details, see Supplementary Information). Also, it is worth noting that between the garnet and the ALD-Al$_2$O$_3$ coating layer, there is a Li-Al-O layer with a typical thickness of 2∼3 nm, as shown in Fig. 3a. This Li-Al-O layer is a transition layer formed between the garnet surface and the Al$_2$O$_3$ layer. The transition Li-Al-O layer was confirmed by EELS results obtained from the Li-Al-O layers at different samples. The EELS data shown in Fig. 3h suggest the presence of Zr, O and La (from garnet) and no Li$_2$CO$_3$ due to the lack of carbon energy loss at ∼284 eV. Meanwhile, the energy loss at 58 eV and 76 eV shown in Fig. 3i can be assigned to the Li K-edge and Al L-edge, respectively, with the Al coming from the ALD deposition.

Neutron depth profiling (NDP) shows a surface Li-ion enrichment layer and adjacent Li depletion zone in garnet due to strong Li segregation in the solid electrolyte (Supplementary Fig. 8). Thus, it is inferred that surface excess Li ions on bare garnet may react with the sensitive trimethyl alumina (TMA) ALD precursor and water at the early ALD nucleation stage, forming a Li and Al oxide layer (denoted as Li-Al-O). With the rapid surface reaction during ALD, Li ions may diffuse out of the garnet surface forming Li-Al-O, followed by regular ALD-Al$_2$O$_3$ deposition on top. Therefore, the ALD treatment on garnet produces a bi-layer structure: Li-Al-O close to the garnet surface, and Al$_2$O$_3$ on top.

The layered structure can be observed in Fig. 3a with what appears to be a subnanometre transition region between the two layers.

SAED was applied to confirm the Li-Al-O layer composition. As shown in Fig. 3j, few rings are present in the electron diffraction pattern, indicating high crystal symmetry of the Li-Al-O structure. Further analysis from the EELS and SAED data suggests that the composition is close to Li$_2$Al$_4$O$_7$ (see the details in Supplementary Fig. 9); however, longer electron-beam irradiation leads to damage of the Li$_2$Al$_4$O$_7$ layer. This layer should be Li-ion conductive. In Fig. 3d,f, it is clearly observed that no Li diffuses into or goes through the pure Al$_2$O$_3$ layer. This result is consistent with the mechanism that Li ion from the garnet surface is consumed to form a Li$_2$Al$_4$O$_7$ layer. In turn, the 40 cycles of ALD-Al$_2$O$_3$ can restrain Li-ion segregation. Note that the samples characterized in Fig. 3 were not heated after ALD treatment. On heating at 250 °C for 60 min, elemental Li was clearly observed to diffuse into and even go through the pure Al$_2$O$_3$ coating layer (Supplementary Fig. 10), which is consistent with the observation in NDP characterization (Supplementary Fig. 11).

Computation of Li metal and garnet interface

To study the interaction between Li metal and garnet after ultrathin ALD coating, first-principles computation was employed. Firstly, the binding energy of Li metal on a lithiated pure ALD-Al$_2$O$_3$ layer with a variety of Li stoichiometry Li$_x$Al$_2$O$_{3+x/2}$ ($x = 0.4$ to 1.4, see Supplementary Information for details) was calculated. The results prove a strong chemical binding between Li metal on Li$_x$Al$_2$O$_{3+x/2}$ ($x = 0.4$ to 1.4) with high binding energies ranging from 6.0 to 11.4 eV nm^{-2}. In turn, this strong interface binding improves the wetting of the Li metal on the Al$_2$O$_3$-coated solid electrolyte. The ultrathin alumina after lithiation is also a good Li-ion conductor and provides effective Li-ion transport paths[37] and low interfacial resistance between Li metal and the garnet. Since garnet electrolytes are typically fabricated in air (which contains CO$_2$), a thin Li$_2$CO$_3$ layer covering the garnet surface is expected (Supplementary Fig. 12 and 13). The interface binding energy between Li metal and the Li$_2$CO$_3$ layer is calculated as 1.6 eV nm^{-2}, which is significantly lower than that between Li and the lithiated alumina (Fig. 4a,b).
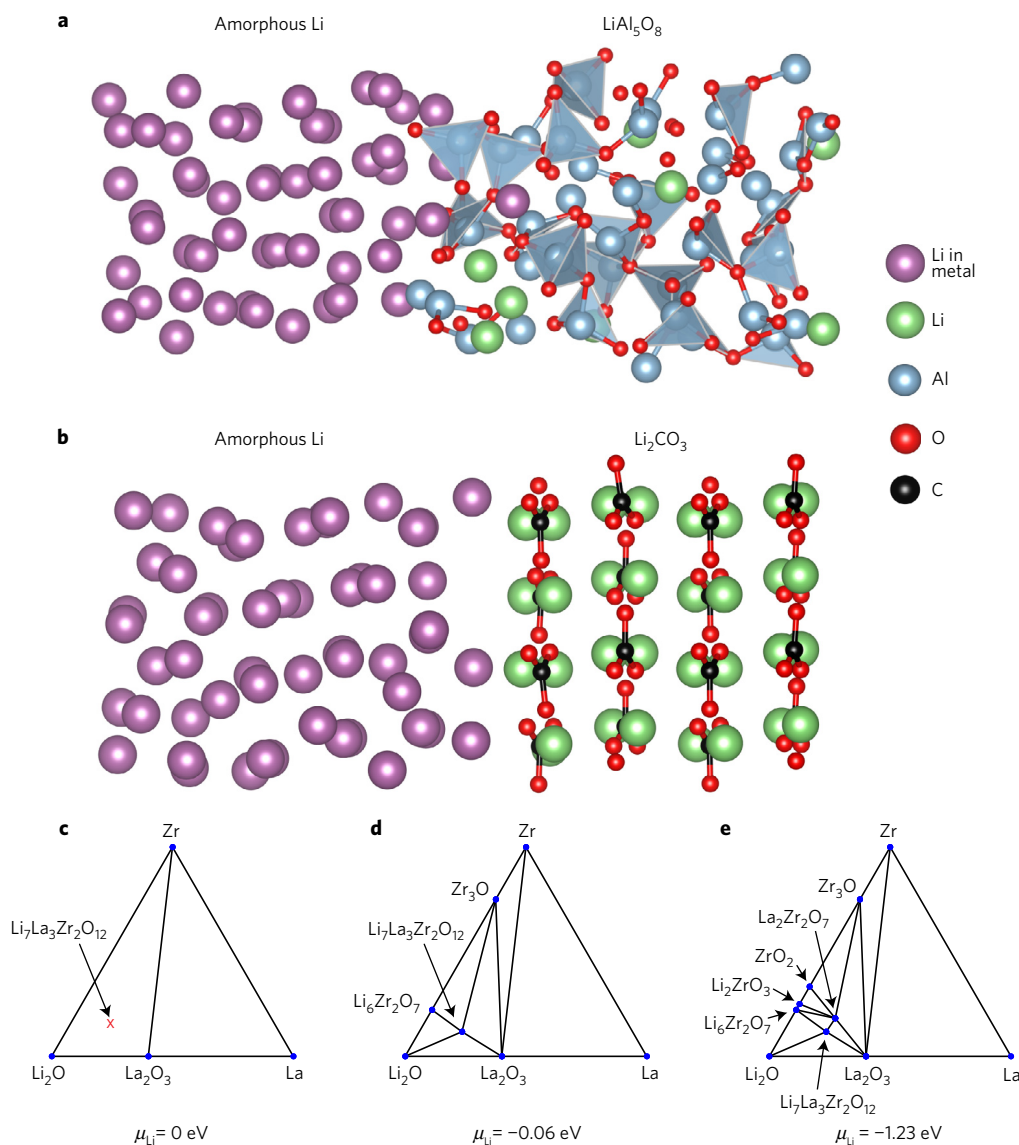
**Figure 4 | First-principles calculations of Li metal and garnet interface with and without ALD-Al$_2$O$_3$. a,b**, The interface model of Li metal on the LiAl$_5$O$_8$ (**a**) and the Li$_2$CO$_3$ (**b**) from *ab initio* molecular dynamics simulations. **c–e**, Li grand potential phase diagrams showing the phase equilibria of a LLZO system at different Li chemical potentials: $\mu_{Li} = 0$ eV, corresponding to Li metal (**c**); $\mu_{Li} = -0.06$ eV (**d**); and -1.23 eV, corresponding to the range of Li chemical potentials in lithiated alumina (**e**).

The weak binding energy leads to low contact area, thus forming gaps and intervals. The existence of gaps and Li$_2$CO$_3$ in the garnet/Li interface would cause large interfacial resistance. This computation result agrees with the notable decrease of interfacial impedance after ultrathin ALD-Al$_2$O$_3$ coating.

Secondly, chemical interfacial stability was also calculated for garnet/Li metal from first principles. On the basis of the Li grand potential phase diagram of the LLZO system (Fig. 4c), a small decomposition energy of -27 kJ mol^{-1} is calculated for the bare cubic LLZO in contact with Li. This decomposition corresponds to a composition of Li$_2$O, Zr and La$_2$O$_3$, indicating a potential tendency for the Li reduction of garnet. Compared to the undoped LLZO, the doped garnet LLCZN used in this study has similar phase stability against Li metal and phase equilibria with additional decomposed compositions, CaO and Nb. The relatively small thermodynamic driving force for the Li reduction of garnet may explain its relative stability against Li metal[46]. At high temperatures (>250 °C), the decomposition of garnet contacting Li metal may proceed and lead to a significant volume expansion up to ~50% on the basis of the

first-principles calculations. This is supported by the experimental evidence of low-angle shifting XRD peaks of LLCZN subjected to heating with Li metal (Supplementary Fig. 2). This large volume expansion localized at the interface may crack the garnet electrolyte and induce a mechanical failure as shown in a previous experimental study[35]. In addition, the decomposition of the garnet electrolyte forms an additional interphase layer similar to solid-electrolyte interphase but with poor Li-ion conductivity. The decomposed materials may contain Li$_2$O/Li$_2$O$_2$, La$_2$O$_3$, Zr/Zr$_x$O, CaO, Nb/NbOx and also possible air contaminations such as Li$_2$CO$_3$ (ref. 33), detrimental for good interfacial ionic conduction. In contrast, the Li grand canonical phase diagram (Fig. 4d,e) indicates that garnet LLZO, similar to the case for LLZCN, is stabilized with lithiated alumina in an equilibrium Li chemical potential (μ_{Li}) window of -0.06 eV to -1.23 eV. Therefore, the introduction of ALD-Al$_2$O$_3$ coating protects garnet from its decomposition via reacting with metallic Li, and maintains a stable, high-conductive interface for garnet electrolyte with Li metal anode. The experimental results on galvanostatic cycling for a long time without an increase of voltage
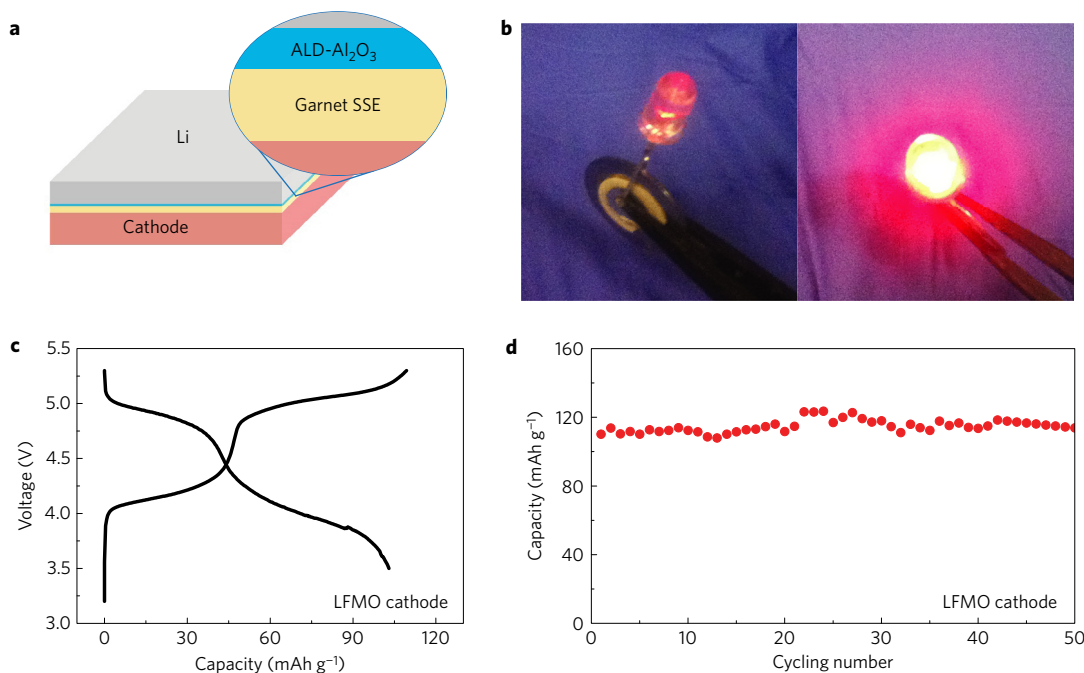
Figure 5 | High-voltage cell with Li metal anode and LLZCN electrolyte. a, Schematic of the designed full cell using ALD-coated LLCZN, Li metal anode, LFMO/carbon black/PVDF composite cathode. Note a tiny amount of liquid organic electrolyte with a composition of 1 M LiPF$_6$ in FEC/FEMC/HFE (20:60:20, by volume) was added to improve the interface between the composite cathode and garnet electrolyte. **b**, A working cell to light up an LED device. The yellowish pellet in the left photo is the ALD-treated LLCZN solid electrolyte. The LED is connected to the cell with the aid of plastic tweezers. **c**, The galvanostatic charge and discharge profile of the LFMO/ALD-garnet SSE/Li full cell. **d**, Cycling performance of the cell.

agree with the computation on the stable interface between Li metal and ALD-coated garnet.

Working cells with Li metal anode and ALD-coated LLCZN

The effective interface between Li metal anode and the garnet electrolyte developed in this work can potentially enable a range of high-energy-density Li-ion batteries. As shown in Fig. 5a, full cells were prepared on the basis of the Li/ALD-treated garnet by using cathode with liquid electrolyte. Since garnet electrolyte is stable up to 6 V, the high-voltage chemistry of Li$_2$FeMn$_3$O$_8$ (LFMO) was selected for a cathode to demonstrate a high-voltage cell. The cathode, comprising LFMO, carbon black, and polyvinylidene fluoride (PVDF, binder), was made by conventional slurry coating on Al foil. A small amount of high-voltage liquid organic electrolyte was added in between the cathode and garnet SSE to reduce the interfacial resistance. The high-voltage organic electrolyte, prepared by dissolving 1.0 M LiPF$_6$ in highly fluorinated solvents, has a high voltage stability over 4.8 V (ref. 47). Figure 5b shows photographs of working cells, which can power a light-emitting diode (LED). The battery was assembled in an argon-filled glovebox and the working cells were packaged into 2032 coin cell cases sealed with epoxy resin. A schematic of the cell assembly is shown in Supplementary Fig. 14. Figure 5c shows the voltage profile of the first cycle at 0.1 C (1 C=150 mA g^{-1}). Clearly, two groups of well-defined plateaux are observed at 4.0 V and 4.9 V for discharge and 4.1 V and 5.0 V for charge, validating the working full cell, and the Li metal anode with a small over-potential (0.1 V). The cell delivered a capacity of 103 mAh g^{-1} (70% theoretical specific capacity of LFMO) with coulombic efficiency of 83% in the first cycle. The cycling performance is shown in Fig. 5d. The charge capacity stabilized around 110 mAh g^{-1} over 50 cycles, demonstrating the feasibility of full cells based on the high-voltage LFMO cathode.

In summary, we report an innovative strategy to solve the interfacial issue between Li metal anode and garnet-type LLCZN

solid electrolyte toward all-solid-state Li batteries. Ultrathin ALD coating of Al$_2$O$_3$ effectively decreased the interfacial ASR from 1,710 Ω cm^2 of the pristine Li/garnet to 1 Ω cm^2 of the stabilized Li/ALD-coated garnet. A working full cell was demonstrated using a high-voltage cathode LFMO, garnet LLCZN, and Li metal anode. The possible mechanism for the interface improvement is proposed on the basis of experimental and computational evidence: the ALD-Al$_2$O$_3$ coating on garnet enables a conformal interface of garnet/Li; the higher binding energy of Li with lithiated alumina further enhances the conformal interface; ultrathin lithiated alumina provides high Li-ion transport paths through the interface; and (4) the Al$_2$O$_3$ coating could possibly prevent garnet decomposition in contact with Li metal, and maintains garnet/Li interface stability and excellent electrical properties. This work has addressed the primary challenge of high interfacial resistance in garnet SSEs with Li metal anodes, and is thus a major breakthrough towards the development of high-energy-density and safe all-solid-state batteries. On the basis of the Li/ALD-treated garnet SSE, we used high-voltage LFMO as the cathode to successfully demonstrate full cells, paving the way to achieve all-solid-state lithium batteries in the future.

Methods

Methods and any associated references are available in the online version of the paper.

References

1. Xu, X. *et al*. Self-organized core–shell structure for high-power electrode in solid-state lithium batteries. *Chem. Mater.* **23,** 3798–3804 (2011).
2. Inada, T. *et al*. All solid-state sheet battery using lithium inorganic solid electrolyte, thio-LISICON. *J. Power Sources* **194,** 1085–1088 (2009).
3. Feng, J. K., Yan, B. G., Liu, J. C., Lai, M. O. & Li, L. All solid state lithium ion rechargeable batteries using NASICON structured electrolyte. *Mater. Technol.* **28,** 276–279 (2013).

4. Noguchi, Y., Kobayashi, E., Plashnitsa, L. S., Okada, S. & Yamaki, J.-I. Fabrication and performances of all solid-state symmetric sodium battery based on NASICON-related compounds. *Electrochim. Acta* **101**, 59–65 (2013).

5. Ihlefeld, J. F. *et al*. Fast lithium-ion conducting thin-film electrolytes integrated directly on flexible substrates for high-power solid-state batteries. *Adv. Mater.* **23**, 5663–5667 (2011).

6. Lü, X. *et al*. Antiperovskite Li_3OCl superionic conductor films for solid-state Li-ion batteries. *Adv. Sci.* **3**, 1500359 (2016).

7. Takahashi, K. *et al*. All-solid-state lithium battery with $LiBH_4$ solid electrolyte. *J. Power Sources* **226**, 61–64 (2013).

8. Trevey, J. E., Jung, Y. S. & Lee, S.-H. High lithium ion conducting $Li_2S–GeS_2–P_2S_5$ glass–ceramic solid electrolyte with sulfur additive for all solid-state lithium secondary batteries. *Electrochim. Acta* **56**, 4243–4247 (2011).

9. Yersak, T. A. *et al*. An all-solid-state Li-ion battery with a pre-lithiated Si–Ti–Ni alloy anode. *J. Electrochem. Soc.* **160**, A1497–A1501 (2013).

10. Buschmann, H. *et al*. Structure and dynamics of the fast lithium ion conductor "$Li_7La_3Zr_2O_{12}$". *Phys. Chem. Chem. Phys.* **13**, 19378–19392 (2011).

11. Djenadic, R. *et al*. Nebulized spray pyrolysis of Al-doped $Li_7La_3Zr_2O_{12}$ solid electrolyte for battery applications. *Solid State Ion.* **263**, 49–56 (2014).

12. Murugan, R., Thangadurai, V. & Weppner, W. Fast lithium ion conduction in garnet-type $Li_7La_3Zr_2O_{12}$. *Angew. Chem. Int. Ed.* **46**, 7778–7781 (2007).

13. Ren, Y. *et al*. Effects of Li source on microstructure and ionic conductivity of Al-contained $Li_{6.75}La_3Zr_{1.75}Ta_{0.25}O_{12}$ ceramics. *J. Eur. Ceram. Soc.* **35**, 561–572 (2015).

14. Thangadurai, V., Schwenzel, J. & Weppner, W. Tailoring ceramics for specific applications: a case study of the development of all-solid-state lithium batteries. *Ionics* **11**, 11–23 (2005).

15. Kamaya, N. *et al*. A lithium superionic conductor. *Nat. Mater.* **10**, 682–686 (2011).

16. Yada, C. *et al*. Dielectric modification of 5 V-class cathodes for high-voltage all-solid-state lithium batteries. *Adv. Energy Mater.* **4**, 1301416 (2014).

17. Takada, K. *et al*. Interfacial phenomena in solid-state lithium battery with sulfide solid electrolyte. *Solid State Ion.* **225**, 594–597 (2012).

18. Sakuda, A. *et al*. All-solid-state lithium secondary batteries with metal-sulfide-coated $LiCoO_2$ prepared by thermal decomposition of dithiocarbamato complexes. *J. Mater. Chem.* **22**, 15247–15254 (2012).

19. Sakuda, A. *et al*. All-solid-state lithium secondary batteries using $Li_2S-P_2S_5$ solid electrolytes and $LiFePO_4$ electrode particles with amorphous surface layer. *Chem. Lett.* **41**, 260–261 (2012).

20. Seino, Y., Ota, T. & Takada, K. High rate capabilities of all-solid-state lithium secondary batteries using $Li_4Ti_5O_{12}$-coated $LiNi_{0.8}Co_{0.15}Al_{0.05}O_2$ and a sulfide-based solid electrolyte. *J. Power Sources* **196**, 6488–6492 (2011).

21. Ohta, N. *et al*. $LiNbO_3$-coated $LiCoO_2$ as cathode material for all solid-state lithium secondary batteries. *Electrochem. Commun.* **9**, 1486–1490 (2007).

22. Kato, T. *et al*. *In-situ* $Li_7La_3Zr_2O_{12}/LiCoO_2$ interface modification for advanced all-solid-state battery. *J. Power Sources* **260**, 292–298 (2014).

23. Ohta, S. *et al*. All-solid-state lithium ion battery using garnet-type oxide and Li_3BO_3 solid electrolytes fabricated by screen-printing. *J. Power Sources* **238**, 53–56 (2013).

24. Van den Broek, J., Afyon, S. & Rupp, J. L. M. Interface-engineered all-solid-state Li-ion batteries based on garnet-type fast Li+conductors. *Adv. Energy Mater.* **6**, 1600736 (2016).

25. Thangadurai, V., Pinzaru, D., Narayanan, S. & Baral, A. K. Fast solid-state Li ion conducting garnet-type structure metal oxides for energy storage. *J. Phys. Chem. Lett.* **6**, 292–299 (2015).

26. Sudo, R. *et al*. Interface behavior between garnet-type lithium-conducting solid electrolyte and lithium metal. *Solid State Ion.* **262**, 151–154 (2014).

27. Ohta, S. *et al*. Co-sinterable lithium garnet-type oxide electrolyte with cathode for all-solid-state lithium ion battery. *J. Power Sources* **265**, 40–44 (2014).

28. Jin, Y. & McGinn, P. J. Bulk solid state rechargeable lithium ion battery fabrication with Al-doped $Li_7La_3Zr_2O_{12}$ electrolyte and $Cu_{0.1}V_2O_5$ cathode. *Electrochim. Acta* **89**, 407–412 (2013).

29. Thangadurai, V., Kaack, H. & Weppner, W. J. F. Novel fast lithium ion conduction in garnet-type $Li_5La_3M_2O_{12}$ (M = Nb, Ta). *J. Am. Ceram. Soc.* **86**, 437–440 (2003).

30. O'Callaghan, M. P., Powell, A. S., Titman, J. J., Chen, G. Z. & Cussen, E. J. Switching on fast lithium ion conductivity in garnets: the structure and transport properties of $Li_{3+x}Nd_3Te_{2−x}Sb_xO_{12}$. *Chem. Mater.* **20**, 2360–2369 (2008).

31. Jalem, R. *et al*. Concerted migration mechanism in the Li ion dynamics of garnet-type $Li_7La_3Zr_2O_{12}$. *Chem. Mater.* **25**, 425–430 (2013).

32. Thompson, T. *et al*. A tale of two sites: on defining the carrier concentration in garnet-based ionic conductors for advanced Li batteries. *Adv. Energy Mater.* **5**, 150096 (2015).

33. Cheng, L. *et al*. The origin of high electrolyte-electrode interfacial resistances in lithium cells containing garnet type solid electrolytes. *Phys. Chem. Chem. Phys.* **16**, 18294–18300 (2014).

34. Kihira, Y., Ohta, S., Imagawa, H. & Asaoka, T. Effect of simultaneous substitution of alkali earth metals and Nb in $Li_7La_3Zr_2O_{12}$ on lithium-ion conductivity. *ECS Electrochem. Lett.* **2**, A56–A59 (2013).

35. Wolfenstine, J., Allen, J. L., Read, J. & Sakamoto, J. Chemical stability of cubic $Li_7La_3Zr_2O_{12}$ with molten lithium at elevated temperature. *J. Mater. Sci.* **48**, 5846–5851 (2013).

36. Jung, S. C. & Han, Y.-K. How do Li atoms pass through the Al_2O_3 coating layer during lithiation in Li-ion batteries? *J. Phys. Chem. Lett.* **4**, 2681–2685 (2013).

37. Jung, S. C., Kim, H.-J., Choi, J. W. & Han, Y.-K. Sodium ion diffusion in Al_2O_3: a distinct perspective compared with lithium ion diffusion. *Nano Lett.* **14**, 6559–6563 (2014).

38. Han, X. *et al*. Atomic-layer-deposition oxide nanoglue for sodium ion batteries. *Nano Lett.* **14**, 139–147 (2013).

39. Wang, D. N. *et al*. Atomic layer deposited coatings to significantly stabilize anodes for Li ion batteries: effects of coating thickness and the size of anode particles. *J. Mater. Chem. A* **2**, 2306–2312 (2014).

40. Lotfabad, E. M. *et al*. Si nanotubes ALD coated with TiO_2, TiN or Al_2O_3 as high performance lithium ion battery anodes. *J. Mater. Chem. A* **2**, 2504–2516 (2014).

41. Kohandehghan, A. *et al*. Silicon nanowire lithium-ion battery anodes with ALD deposited TiN coatings demonstrate a major improvement in cycling performance. *J. Mater. Chem. A* **1**, 12850–12861 (2013).

42. Li, Y. *et al*. Tuning electrochemical performance of Si-based anodes for lithium-ion batteries by employing atomic layer deposition alumina coating. *J. Mater. Chem. A* **2**, 11417–11425 (2014).

43. Liu, T. *et al*. Achieving high capacity in bulk-type solid-state lithium ion battery based on $Li_{6.75}La_3Zr_{1.75}Ta_{0.25}O_{12}$ electrolyte: interfacial resistance. *J. Power Sources* **324**, 349–357 (2016).

44. Sharafi, A., Meyer, H. M., Nanda, J., Wolfenstine, J. & Sakamoto, J. Characterizing the $Li–Li_7La_3Zr_2O_{12}$ interface stability and kinetics as a function of temperature and current density. *J. Power Sources* **302**, 135–139 (2016).

45. Tsai, C. L. *et al*. $Li_7La_3Zr_2O_{12}$ interface modification for Li dendrite prevention. *ACS Appl. Mater. Interfaces* **8**, 10617–10626 (2016).

46. Mo, Y., Ong, S. P. & Ceder, G. First principles study of the $Li_{10}GeP_2S_{12}$ lithium super ionic conductor material. *Chem. Mater.* **24**, 15–17 (2012).

47. Zhang, Z. *et al*. Fluorinated electrolytes for 5 V lithium-ion battery chemistry. *Energy Environ. Sci.* **6**, 1806–1810 (2013).

Author contributions

X.H., Y.G. and K.F. fabricated the samples and carried out the experiments, characterizations, data analysis, and manuscript preparation. X.H. and Y.M. conducted the theoretical analysis. G.T.H. helped prepare samples and analysed the experimental results. J.D. drew the schematics and prepared FIB samples. A.P. and G.R. carried out the XPS and XPS data analysis. B.L. prepared samples and conducted ALD. H.W. carried out NDP and NDP data analysis. V.T. helped review the results, and E.D.W. and L.H. managed the project and reviewed the results, data analysis, and manuscript preparation.

Additional information

Supplementary information is available in the online version of the paper. Reprints and permissions information is available online at www.nature.com/reprints.
Correspondence and requests for materials should be addressed to E.D.W. or L.H.

Competing financial interests

The authors declare no competing financial interests.

Methods

Materials synthesis. The LLCZN garnet electrolyte was synthesized via a sol-gel method. The starting materials were La(NO$_3$)$_3$ (99.9%, Alfa Aesar), ZrO(NO$_3$)$_2$ (99.9%, Alfa Aesar), LiNO$_3$(99%, Alfa Aesar), NbCl$_5$ (99.99%, Alfa Aesar) and Ca(NO$_3$)$_2$ (99.9%, Sigma Aldrich). Stoichiometric amounts of chemicals were dissolved in de-ionized water and 10% excess LiNO$_3$ was added to compensate for lithium volatilization during high-temperature synthesis. Citric acid and ethylene glycol in the molar ratio of 1:1 were consequently added into the solution. The solution was slowly evaporated on a hotplate to produce the precursor gel with stirring, which was then heated to 400 °C for 10 h to burn out the organics. After this, the obtained powder was ball-milled and pressed into pellets for calcination at 800 °C for 10 h. The synthesized powders were then uniaxially pressed into pellets, which were sintered at 1,050° for 12 h in alumina boats covered with the same powder.

Characterization. Scanning electron microscopy was performed with a Hitachi SU-70 analytical scanning electron microscope. The phase analysis was performed with powder X-ray diffraction on a D8 Advanced with LynxEye and SolX (Bruker AXS) using a Cu Kα radiation source operated at 40 kV and 40 mA. Transmission electron microscopy (TEM) was performed on the JEOL 2100f field-emission transmission electron microscope equipped with an electron energy-loss spectroscopy system (TRIDIEM). To prepare the TEM sample, a TESCAN GAIA focused ion beam (FIB) and Fischione 1010 ion milling were used to cut out garnet samples. Before cutting, 10 nm Ti via electron-beam evaporation was deposited onto samples to protect the atomic layer deposition (ALD) layer from being damaged during the cutting process. XPS was applied to study the surface chemistry of the garnet surface with and without ALD-Al$_2$O$_3$ coating. Data were collected with a monochromatic Al X-ray source in a Kratos Ultra DLD tool. Survey spectra were collected using a 12 kV monochromatic Al Kα X-ray source in hybrid lens mode with a step size of 1 eV and pass energy of 160 eV. High-resolution spectra were collected using a 12 kV monochromatic Al Kα X-ray source in hybrid lens mode with a step size of 0.1 eV and pass energy of 20 eV. All peak locations in this data are referenced to the hydrocarbon peak in the C$_{1s}$ spectra, which is calibrated to be at 284.8 eV. High-resolution data were collected with a pass energy of 20 eV, and peak fits performed using CasaXPS software. The near-surface Li depth profiles of garnet from various preparation histories were examined using neutron depth profiling (NDP). NDP spectra were acquired at the NG1 Cold Neutron Depth Profiling station at the NIST Center for Neutron Research (NCNR). The entire specimen was irradiated at a constant fluence rate of cold neutrons, with wavelengths in the range of 0.4–2 nm. The Li composition was calculated using the stopping power of the stoichiometric composition of metal oxide and a standard specimen with known Li abundance.

Atomic layer deposition for LLCZN electrolyte pellets. The ALD was performed with a Beneq TFS 500 for Al$_2$O$_3$ deposition. High-purity nitrogen at 150 °C was used as carrier gas for the whole process. Typically, for 5–6 nm Al$_2$O$_3$ coating, 40 ALD cycles were performed. Each cycle included alternating flows of trimethylaluminum (TMA, 4 s, Al precursor) and water (4 s, oxidant) separated by flows of pure nitrogen gas (4 and 10 s, respectively, carrier and cleaning gas). For estimation, we carried out the control test for the ALD system on a clean Si wafer, and the average thickness for each ALD cycle was 0.1297 nm. Thus, 40 cycles is estimated as 5.2 nm (40 × 0.1297 nm ≈ 5.2 nm), agreeable with the measurement from the TEM image (5∼6 nm in Fig. 3a).

Assembly of Li metal coated LLCZN. A thin Li foil disc (0.8 cm in diameter and 0.2 mm thick) was put on ALD-Al$_2$O$_3$-treated LLCZN pellets in a glovebox filled with ultrahigh-purity Ar, and then the stacked Li/LLCZN pellet was heated at 250 °C for 60 min with a pressure of 0.26 psi by 6 stainless-steel discs (1.5 g each). The small pressure was used to help the initial contact of melted lithium on the garnet surface. For control, freshly polished LLCZN pellets were assembled with

lithium metal via the same procedure. After cooling down to room temperature, the thin lithium disc was stuck on the pellets. Scanning electron microscopy was performed for the samples' cross-section obtained by breaking with tweezers.

Synthesis of Li$_2$FeMn$_3$O$_8$ (LFMO). LFMO was synthesized according to the literature[48] with modification. Briefly, glycine–nitrate mixture solution was firstly prepared by dissolving lithium nitrate, iron nitrate, manganese nitrate (2:1:3, molar ratio) and glycine in de-ionized water. The molar ratio of nitrate to glycine is 2:1. Then, the LFMO powder was obtained by combustion reaction of the glycine–nitrate solution at 300 °C, followed by a 2-h annealing at 700 °C.

First-principles calculations. First-principles calculations were performed using the Vienna Ab initio Simulation Package (VASP) within the projector augmented-wave approach with the Perdew–Burke–Ernzerhof generalized-gradient approximation to density functional theory. The materials entries for the grand potential phase diagram were obtained from the Materials Project database[49]. The interface models comprising a slab of amorphous Li metal and a slab of the Li$_2$CO$_3$ or the lithiated alumina were equilibrated using *ab initio* molecular dynamics simulations at 513 K for 30 ps. The binding energy was calculated as the energy of the interfaces minus the energy of the separated surface slabs.

Battery assembly and electrochemical tests. To measure the ionic conductivity of the garnet solid-state electrolyte, Au paste was coated on both sides of the ceramic disc and acted as a blocking electrode. The gold electrodes were sintered at 700 °C to form good contact with the ceramic pellet. The EIS was performed over a frequency range of 1 MHz to 100 mHz with a 50 mV perturbation amplitude. Owing to the sensitivity of Li metal to oxygen and moisture, all of the cells including symmetric cells and full cells were assembled and tested in an ultrahigh-purity-argon (99.999%)-filled glovebox with moisture and oxygen levels below 0.1 and 0.01 p.p.m., respectively. In a typical LLCZN/Li assembly, Li foil was pressed to about 0.2 mm, and then punched into thin discs with a diameter of 0.79 cm. The thin Li foil disc was spread and gently pressed on ALD-Al$_2$O$_3$-coated LLCZN pellets at one or both sides with a pair of plastic tweezers. Six pieces of stainless steel (9 g in total) were put on the Li foil. Then the stacked Li/ALD-Al$_2$O$_3$/Li cell was put in an oven in the glovebox, which was then heated at 250 °C for 1 h, followed by natural cooling down to room temperature. The LLCZN/Li was then ready to use. The stainless steel was used as the current collector. The cathode discs were made outside the glovebox. The as-synthesized LFMO was thoroughly mixed with carbon black and PVDF at a mass ratio of 80:10:10 in NMP (solvent, N-methyl-2-pyrrolidone). The mixture was then coated on a clean and flat Al foil. After drying in air, the Al foil with the cathode slurry coated was put in a vacuum oven and further dried overnight at 110 °C. It was then punched into cathode discs (diameter of 0.79 cm). The mass measurement was done with a microbalance (Sartorius). The full cells were assembled by putting the cathode disc on the bare side of the Li/ALD-Al$_2$O$_3$-LLCZN pellet with a tiny amount of high-voltage organic liquid electrolyte added between the cathode and the LLCZN pellet. The cells were packaged in 2032 coin cell cases and the edge of the cells was sealed by epoxy resin. They were kept in a glovebox during all tests. The tests were carried out with a BioLogic battery tester at room temperature via a feedthrough in the glovebox. The cut voltages were 3.5 V and 5.3 V with a current density of 0.1 C (1 C=150 mA g^{-1}).

References

48. Kawai, H., Nagata, M., Tabuchi, M., Tukamoto, H. & West, A. R. Novel 5 V spinel cathode Li$_2$FeMn$_3$O$_8$ for lithium ion batteries. *Chem. Mater.* **10,** 3266–3268 (1998).
49. Jain, A. *et al*. Commentary: the Materials Project: a materials genome approach to accelerating materials innovation. *APL Mater.* **1,** 011002 (2013).